

Revealing the Role of Active Fillers in Li-ion Conduction of Composite Solid Electrolytes

Shida Xue, Shiming Chen, Yanda Fu, Hengyao Zhu, Yuchen Ji, Yongli Song, Feng Pan,* and Luyi Yang*

Composite solid electrolytes (CSEs) consisting of polyethylene oxide (PEO) matrix and active inorganic fillers have shown great potential for practical applications. However, mechanisms of how different active fillers enhance ion transport in CSEs still remain inconclusive. In this work, the component dependencies of ionic conductivity of PEO-based CSEs are investigated by comparing two widely investigated active fillers: NASICON-type (LATP) and garnet-type (LLZTO). In terms of ionic conductivity, the optimum ratios are strikingly different for LLZTO (10 wt%) and LATP (50 wt%). Through experimental and computational studies, it is demonstrated that the high affinity between LATP and PEO facilitates unhindered interfacial Li+ transfer so that LATP functions as a bulk-active filler to provide additional inorganic ion pathways. By contrast, Li⁺ transfer between LLZTO and PEO is found to be sluggish. Instead, LLZTO mainly improves ionic conductivity by dissociating lithium salt, making it a surface-active filler. Through categorizing active fillers based on their Li+ conductive mechanisms, this work provides new understanding and guidelines for componential design and optimization of solid composite electrolytes.

1. Introduction

Exhibiting satisfactory safety and high energy density, all-solid-state lithium-ion batteries (ASSLBs) are considered the next-generation energy storage device for green power. [1,2] As a key component in ASSLBs, solid-state electrolytes (SSEs) SSE can be divided into inorganic solid electrolytes (ISEs) and solid polymer electrolytes (SPEs). [3–5] Oxide-based ISEs such as perovskite $\text{Li}_{3.3}\text{La}_{0.56}\text{TiO}_3$, NASICON $\text{Li}_{1.3}\text{Al}_{0.7}\text{Ti}_{1.3}$ (PO₄) $_3$ (LATP) and garnet $\text{Li}_7\text{La}_3\text{Zr}_2\text{O}_{12}$ (LLZO) are widely investigated due to their high conductivity ($10^{-4}-10^{-3}~\text{S}\cdot\text{cm}^{-1}$). However, poor interfacial

S. Xue, S. Chen, Y. Fu, H. Zhu, Y. Ji, F. Pan, L. Yang School of Advanced Materials Peking University Shenzhen Graduate School Shenzhen 518055, China E-mail: panfeng@pkusz.edu.cn; yangly@pkusz.edu.cn Y. Song School of Energy and Power Engineering Jiangsu University Zhenjiang 212013, China

The ORCID identification number(s) for the author(s) of this article can be found under https://doi.org/10.1002/smll.202305326

DOI: 10.1002/smll.202305326

contacts resulting from their rigid nature limit their further application. [6-9] By contrast, SPEs with coordinating ether-oxygen (-EO) groups in the main chain (e.g., polyethylene oxide, PEO) preserve outstanding flexibility and superior electrodewetting ability, but the relatively low room-temperature conductivity and lack of mechanical strength have become the fatal bottleneck. [10-12]

To overcome the intrinsic issues of ISEs and SPEs, composite solid electrolytes (CSEs) derived from the incorporation of PEO polymer matrix and ion-conductive active ceramic fillers offer a new path toward both high ionic conductivity and good mechanical properties. [13,14] Although previous studies have confirmed the enhanced ion transportation in CSEs including PEO-LLZO and PEO-LATP, the research on the relevant mechanism is still lacking and remains controversial. [15,16] Zheng et al. have traced the Li⁺ transportation in PEO-LLZO composite electrolytes by solid-state NMR

and suggested that Li⁺ transfer mainly through LLZO ceramic fillers once percolated network formed by connected inorganic particles.^[17,18] Instead, Li et al. have attributed the fast ionic conduction in PEO:Ga-LLZO composite to the continuous space charge region at the interface of PEO and LLZO fillers.^[19] As for PEO-LATP composite system, Wang et al. have proved that the restructured region at PEO/LATP interface contributed to accelerating Li⁺ transportation.^[20] while other researchers have proposed an additional pathway through the ceramic bulk for ion conduction.^[21,22] Therefore, direct experimental evidence and computational results are needed to reveal the ion transportation mechanism in CSEs.

In this work, CSEs are prepared by the integration of PEO matrix and nano-sized LATP and Ta-doped LLZO (LLZTO) active fillers (300 nm), and the ionic conductivity dependence on electrolyte composition is brought to light. Based on the analysis of Li⁺ transport across polymer/ceramic interface, we have access to a new understanding of the ion-conducting mechanism for composite electrolyte: LATP serves as bulk-active ceramic for Li⁺ transfer, whereas surface-active LLZTO improves the ion transport by promoting Li salt dissociation. The key principles proposed in this work could be adopted to design high-performance CSEs in ASSLBs.

16136829, 2023, 46, Downloaded from https://onlinelibrary.wiley.com/doi/10.1002/smll.20230326 by University Town Of Shenzhen, Wiley Online Library on [23/11/2025]. See the Terms and Conditions (https://onlinelibrary.wiley.com/terms-and-conditions) on Wiley Online Library for rules of use; OA articles are governed by the applicable Creative Commons Licenses

www.small-journal.com

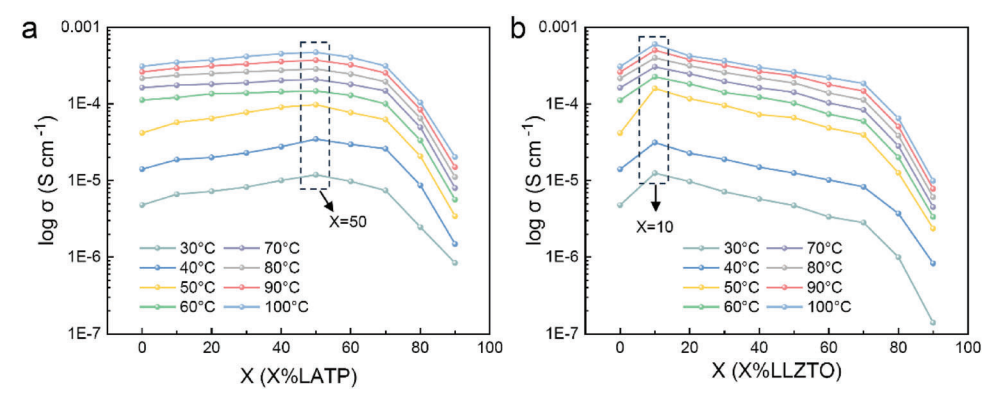


Figure 1. a) Ionic conductivity dependence of PEO-LATP and b) PEO-LLZTO on filler content from 30 °C to 100 °C.

2. Results and Discussion

2.1. Ionic Conductivity Dependence on CSE Compositions

LATP and LLZTO active filler with an average size of 300 nm (Figure S1, Supporting Information) and similar morphologies (Figure S2, Supporting Information) are employed to fabricate PEO-LATP and PEO-LLZTO CSEs. The X-ray diffraction pattern presented in Figure S3 (Supporting Information) confirms the crystalline information of both LATP and LLZTO.[4,23] PEO-LATP/LLZTO CSEs with various filler ratios from 0 wt% to 90 wt% are obtained by casting method. For brevity, PEO-LATP and PEO-LLZTO composite with different filler content are denoted as PEO-xLA and PEO-xLL (x = 10, 20...90). The ionic conductivities of PEO-LATP and PEO-LLZTO at different temperatures are determined with electrochemical impedance spectra (EIS). To explore the influence of active filler content on ionic transportation of CSEs, the correlation between ionic conductivity and ceramic weight ratios are presented in Figure 1a,b, where contrasting trends of Li+ conductivity variation with filler content can be observed. The conductivity of PEO-LATP increases with filler content and peaks at PEO-50LA, followed by a downtrend beginning from PEO-60LA.[24] Unlike PEO-LATP CSEs, significant improvement of conductivity is observed for PEO-10LL, but a decreasing trend starts from a low filler content of merely 20 wt%.[25] Moreover, corresponding Arrhenius curves are also different (Figure S4, Supporting Information), suggesting different Li+ transfer mechanisms between two CSEs.

Based on above variation curves, it can be concluded that the ionic conductivity of PEO-LA peaks at the medium-filler-content region while PEO-LL shows the highest value at the low-filler-content region. Despite both LLZTO and LATP are defined as active fillers, their significantly different Li⁺ conducting behaviors raises a question: can active fillers be further categorized according to their functioning mechanisms in improving Li⁺ conductivity.

2.2. Ion Transportation Across Polymer/Ceramic Interface

To verify the above findings, sandwich-like PEO-LATP/LLZTO-PEO electrolytes (**Figure 2**a) were fabricated to directly evaluate the interfacial ion transfer between PEO and both ISEs. It has been reported that the Li₂CO₃ residues formed at the surface of

LLZO during annealing prevent Li⁺ transport from polymer to LLZO bulk. [26,27] Therefore, both ceramic pellets were polished carefully and Li₂CO₃ was successfully removed from the surface according to the Fourier transform infrared spectra (FTIR, Figure S5, Supporting Information). The obtained LLZTO and LATP pellets exhibit high ionic conductivity of $1.02 \times 10^{-3}~\rm S\cdot cm^{-1}$ and $5.75 \times 10^{-4}~\rm S\cdot cm^{-1}$ at 30 °C, respectively (Figure S6, Supporting Information), which are consistent with previous results. [28,29]

Nyquist plots (Figure S7, Supporting Information) and the corresponding Arrhenius plots (Figure 2b) of PEO-LL-PEO and PEO-LA-PEO at various temperatures show that the ionic conductivity of PEO-LA-PEO is much higher than PEO-LL-PEO despite the higher ionic conductivity of LLZTO pellet. To investigate the origin of such ion conduction discrepancy, Nyquist plots of the above cells are fitted with corresponding equivalent circuits (Figure S8, Supporting Information) to decouple the overall resistance into interfacial resistance (R_{int} , corresponding to medium frequencies) and bulk resistance (R_{bulk} , corresponding to high frequencies). $^{[30,31]}$ The detailed values of $R_{\rm int}$ and $R_{\rm bulk}$ are listed in Table S1 (Supporting Information). Herein, two typical working temperatures (30 and 60 °C) for PEO-based CSEs are selected as representative examples. As the proportional distribution of R_{bulk} and R_{int} displayed in Figure 2c, huge interfacial R_{int} (9734.01 Ω ·cm⁻² at 30 °C and 613.12 Ω ·cm⁻² at 60 °C) of PEO-LL-PEO account for over 85% of the total resistance, resulting in low ionic conductivity at 30°C (1.21 \times 10⁻⁵ S·cm⁻¹) and 60 °C (1.90 \times 10⁻⁴ S·cm⁻¹). In contrast, owing to the lower $R_{\rm int}$ (834.54 Ω ·cm⁻² at 30°C and 61.71 Ω·cm⁻² at 60 °C), much higher overall ionic conductivity of $7.05 \times 10^{-5} \text{ S} \cdot \text{cm}^{-1}$ at 30 °C and $9.67 \times 10^{-4} \text{ S} \cdot \text{cm}^{-1}$ can be obtained for PEO-LA-PEO at 30 °C and 60 °C, respectively.

The sluggish ion transport across PEO/LLZTO interface is further confirmed by the activation energy (E_a) calculation for both PEO/LATP and PEO/LLZTO interfaces based on the interfacial ionic conductivity $\sigma_{\rm int}$ (Figure 2d).^[32] The high E_a (0.704 eV) for PEO/LLZTO interface suggests unfavorable Li⁺ transfer kinetics between organic and inorganic phases so that the LLZTO particles are practically isolated from PEO domains by highly-resisting interface.^[33] Therefore, the ion conduction deteriorates for PEO-LL with medium filler contents because excessive LLZTO particles not only lower the relative content of PEO but also hinder the segmental motion of PEO matrix. In comparison, exhibiting favorable E_a (0.595 eV), Li⁺ has facile access to passing through LATP ceramic in PEO-LA instead of taking a "detour" around

.com/doi/10.1002/smll.202305326 by University Town Of Shenzhen, Wiley Online Library on [23/11/2025]. See the Terms and Conditions (https://onlinelibrary.wiley.com/terms

onditions) on Wiley Online Library for rules of use; OA articles are governed by the applicable Creative Commons I

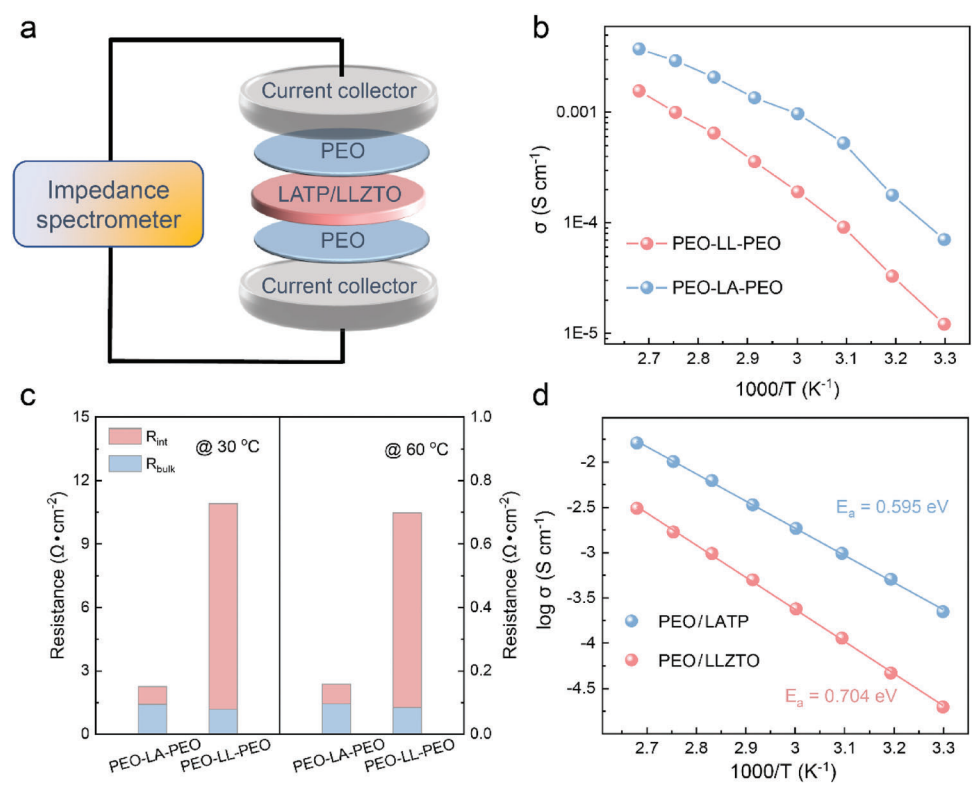


Figure 2. a) Schematic of the multilayer cell configuration. b) Arrhenius plots of PEO-LA-PEO and PEO-LL-PEO. c) Proportional distribution of R_{bulk} and R_{int} of PEO-LA-PEO and PEO-LL-PEO at 30 and 60 °C. d) Arrhenius plots of PEO/LATP and PEO/LLZTO interface.

ceramic particles. Consequently, PEO-LA CSEs benefit from a well-constructed ion conducting network in PEO-LA at medium-filler-content region.

2.3. The Affinity Between PEO and LATP

To explore the origin of the difference in interfacial resistance between PEO and ceramic, computational simulations are performed to evaluate the energy barriers of Li+ decoupling from PEO chains (for the convenience of simulation, diglyme molecules are adopted in calculation as a similar analogy) and diffuse into the bulk of active fillers in the CSEs. As illustrated in Figure 3a, the process can be described as follow: $\operatorname{Li^{+}}$ is first decoupled from one PEO chain after another (process of i→ii and ii→iii), followed by the desolvated Li⁺ diffuse into the ceramic bulk (process of iii→V). It can be inferred from the calculated results (Figure 3b,c) that the lower energy barriers for PEO-LATP than PEO-LLZTO during the process of i→iii boost the ion-decoupling from PEO chains.^[19,36] As for the process of iii→iV, naked Li⁺ also exhibits a lower energy barrier to transport through the surface of LATP (0.21 eV) compared with LLZTO (0.26 eV). Combining with the EIS results obtained in Figure 2, it can be inferred that LATP accelerates interfacial Li⁺ transfer for PEO-LATP due to the more favorable Li⁺-decoupling process as well as the favorable kinetics passing through LATP surface.

Fourier transform infrared spectroscopy (FTIR) characterization is also employed to investigate the chemical environment of PEO-ceramic interfaces (Figure 3d). The absorption band in

the region of 670–625 cm⁻¹ assigned to the P–O bending vibration of LATP shifted to high wavenumbers after compositing with PEO, which is induced by the interaction with electron-withdrawing ethylene oxide groups. The peak shift increases with the content of PEO, suggesting intensified interactions. By contrast, LLZTO shows no peak shift upon compositing with PEO, indicating much weaker interfacial interaction (Figure 3e). It can be inferred that PEO shows much higher interfacial affinity toward LATP than LLZTO, so the PEO-coordinated Li⁺ could move closer to LATP, hence the improved desolvation kinetics for Li⁺.

To obtain further information regarding the interfacial affinity in PEO-LATP and PEO-LLZTO, small-angle x-ray scattering (SAXS) tests (Figure 3f,g) were carried out to evaluate the phase separation.^[35] The scattering intensity of PEO-10LL sharply increases, corresponding to a higher phase separation; whereas the value for PEO-10LA barely changed. Interestingly, PEO-50LA exhibits similar scattering intensities with PEO-10LL and shows a much more uniform compositional distribution than PEO-50LL. Nevertheless, under a high filler weight content of 70 wt%, both CSEs PEO-70LA and PEO-70LL fail to maintain a homogeneous phase, thus the drastic drop in ionic conductivity of the CSEs (Figure 1a,b). Moreover, the contact angle of liquid Polyethylene glycol (PEG) on LATP and LLZTO pellet further confirms such interfacial affinity (Figure S9, Supporting Information): A smaller contact angle of 48.9° is observed on LATP in comparison to 57.7° on LLZTO, implying strong affinity between PEO and LATP. From the above results, it can be concluded that owing to the strong affinity between PEO and LATP, a medium amount of LATP filler will not cause apparent phase separation. In

wellbrary.wiley.com/doi/10.1002/smll.202305326 by University Town Of Shenzhen, Wiley Online Library on [23/1/2025]. See the Terms and Conditions (https://www.com/doi/10.1002/smll.202305326 by University Town Of Shenzhen, Wiley Online Library on [23/1/2025]. See the Terms and Conditions (https://www.com/doi/10.1002/smll.202305326 by University Town Of Shenzhen, Wiley Online Library on [23/1/2025]. See the Terms and Conditions (https://www.com/doi/10.1002/smll.2025).

/onlinelibrary.wiley.com/terms-

conditions) on Wiley Online Library for rules of use; OA articles are governed by the applicable Creative Commons License

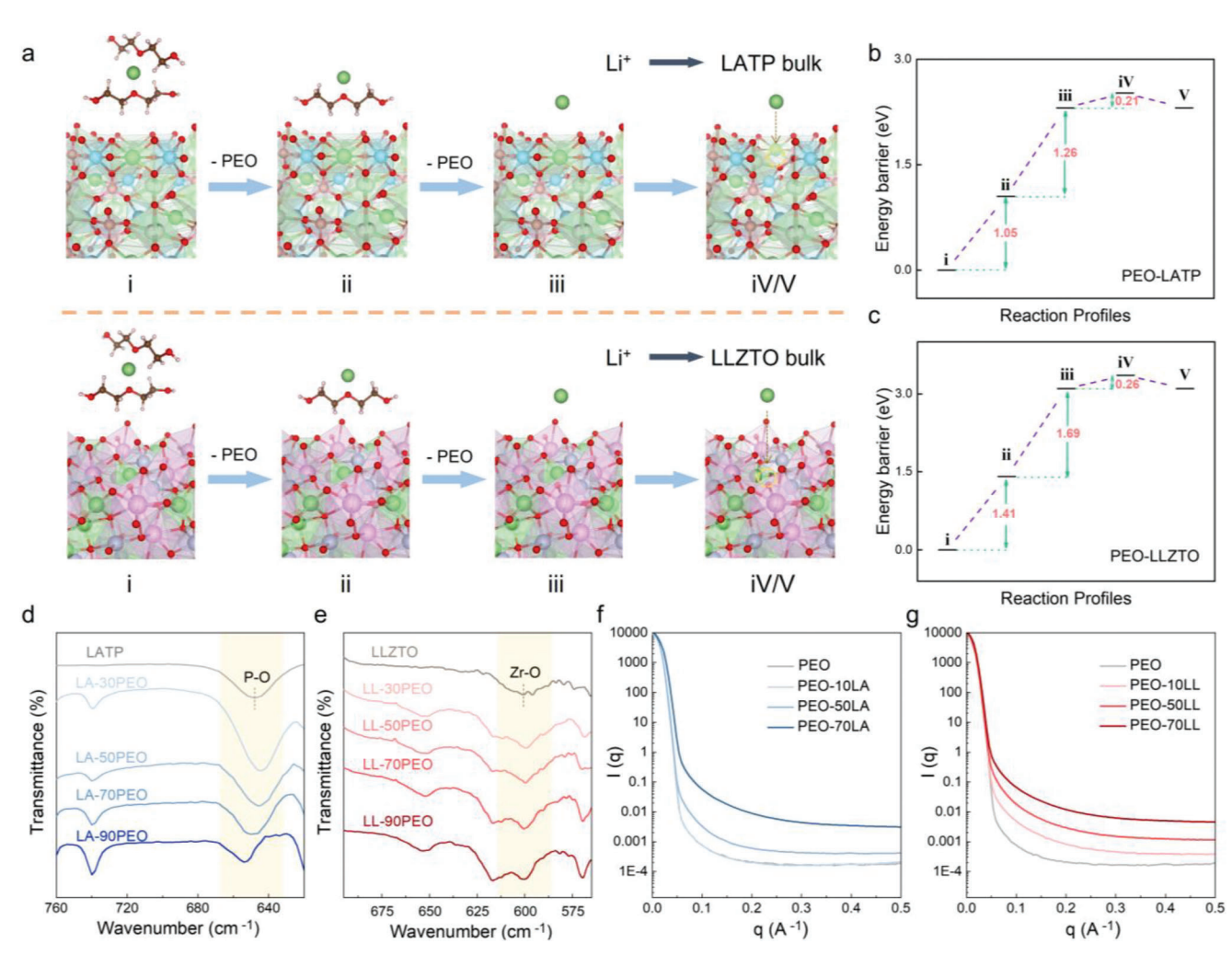


Figure 3. a) Schematic of a computational model for Li⁺ transportation from PEO chains to ceramic bulk. b) Energy barriers of Li⁺ transfer from PEO to LATP bulk. c) Energy barriers of Li+ transfers from PEO to LLZTO bulk. Infrared spectra of d) PEO-LATP and e) PEO-LLZTO CSEs. SAXS profiles of f) PEO-LATP and g) PEO-LLZTO CSEs.

comparison, a medium content of LLZTO causes severe phase separation in PEO due to the incompatible interface, leading to particle aggregation and a discontinuous Li+ conduction pathway. As for high-filler-content CSEs, the amount of PEO is too low to cover the surface of both LATP and LLZTO, not to mention maintaining the structural homogeneity of the CSE.

2.4. Li-Salt Dissociation Effect of LLZTO to Boost Ion Transport

Despite the highly-resistive interface insulating inter-phase ion transfer in PEO-LL, PEO-10LL exhibits the highest ionic conductivity among all the tested CSEs. Therefore, it is equally crucial to unveil the promoting mechanism of LLZTO on ionic conductivity. The Arrhenius plot of PEO, PEO-10LL, and PEO-10LA (Figure 4a) shows a combination of Arrhenius and Vogel-Tammann-Fulcher (VTF) behaviors.[36] The Arrhenius behavior refers to ion hopping decoupled from long-range motions of the crystallized PEO matrix while VTF behavior is related to ion motion coupled with long-range motions of the polymer chains. For CSEs systems, the transition between the two modes occurs at the melting temperature (T_m) : below T_m , Arrhenius behavior predominates due to the immobilized crystalline PEO chains; above $T_{\rm m}$, VTF behavior takes place owing to the high mobility of chain segments. The transition temperature of the CSEs locates at 51.9, 59.5, and 60.6 °C for PEO-10LL, PEO-10LA, and PEO respectively, indicating the lowest melting temperature of PEO-10LL. Considering the plasticizing effect of lithium salt on PEO, [37] differential scanning calorimetry (DSC) tests of the CSEs with and without LiTFSI are performed to explore the influence of LATP and LLZTO on the motion of polymer chains. Without LiTFSI, the PEO-LA composite shows the lowest T_m (65.3 °C), indicating that LATP has a greater impact on reducing crystallinity of PEO than LLZTO, which may attribute to the specific affinity as mentioned above (Figure 4b). However, after the addition of LiTFSI, the T_m of PEO-10LL decreases to 54.2 °C, lower than that of PEO-10LA (Figure 4c). According to analogous observations in previous studies, it can be speculated that LLZTO disrupts the crystallinity of PEO chains by promoting the dissociation of Li-salts.[38,39] This dissociation effect is proved by FTIR results

www.small-journal.com

16136829, 2023, 46, Downloaded from https://onlinelibrary.wiley.com/doi/10.1002/smll.202305326 by University Town Of Shenzhen, Wiley Online Library on [23/112025]. See the Terms and Conditions (https://onlinelibrary.wiley.com/terms

xonditions) on Wiley Online Library for rules of use; OA articles are governed by the applicable Creative Commons License

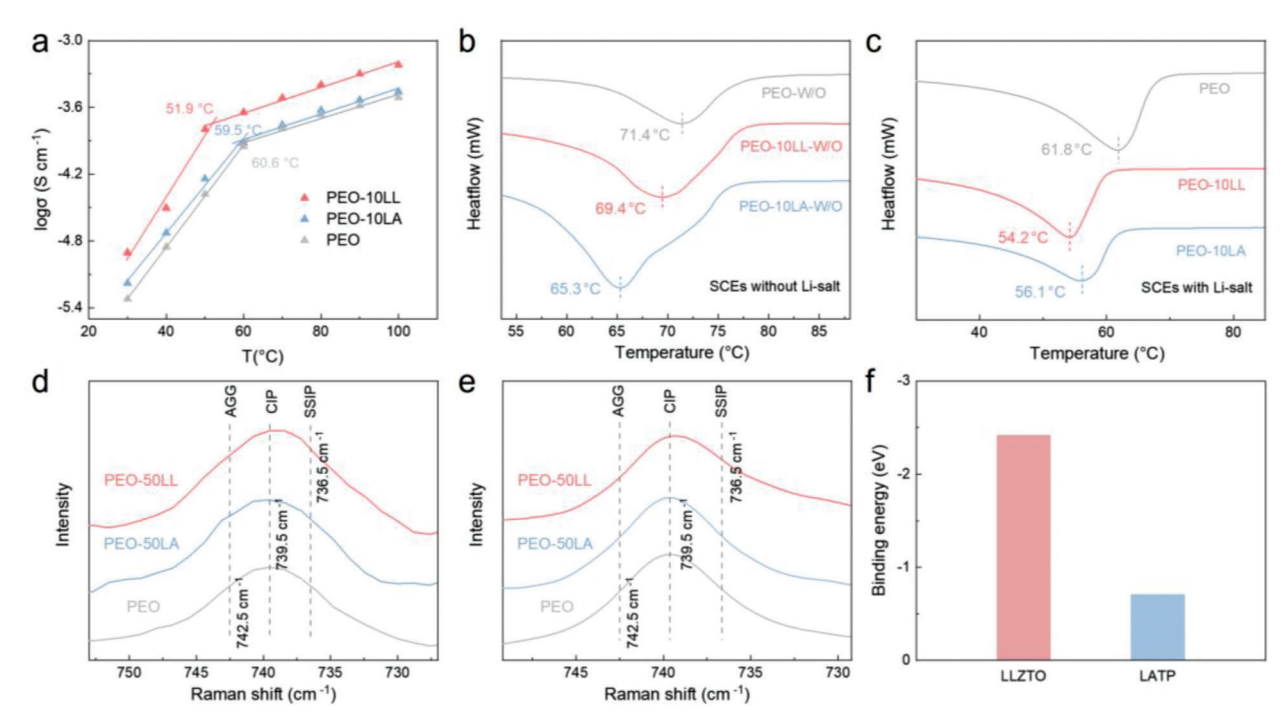


Figure 4. a) Arrhenius plots of PEO, PEO-10LA and PEO-10LL. DSC curves of PEO, PEO-10LA, PEO-10LL b) with Li-salt and c) without Li-salt. d) FTIR profiles and e) Raman spectra of PEO, PEO-50LA, and PEO-50LL. f) Simulated binding energy between TFSI⁻ anion and the surface of different fillers.

(Figure 4d), where the characteristic peak located at 742.5, 739.5, and 736.5 cm⁻¹ can be assigned to aggregates (AGGs), contact ion pair (CIP) and solvent-separated ion pair (SSIP) of the Li⁺-TFSI⁻ pair.^[40] The proportion of SSIP in PEO-LL is higher than that in PEO-LA and PEO, confirming the promoted LiTFSI dissociation in the presence of LLZTO. Similar conclusions can also be drawn from Raman spectra (Figure 4e), where the ratio of SSIP in PEO-LL outweighs others.^[39] Since DSC profiles of PEO-LL composites with various filler contents also confirm PEO-10LL has the lowest melting point (Figure S10, Supporting Information), it can be speculated the improved ionic conductivity of PEO-LL originates from Li-salt dissociation.

To explore the relevant promoting mechanism of LLZTO, computational simulation is conducted to evaluate the dissociation effect on both LLZTO and LATP (Figure S11, Supporting Information). As presented in Figure 4f, the binding energy between TFSI $^-$ and LATP is -0.71 eV, while the binding energy at LLZTO surface is -2.42 eV, suggesting an anchoring effect of TFSI $^-$ on the surface of LLZTO. This result could be attributed to the abundant Lewis acid existing on LLZTO surface, which functions as trapping sites for TFSI $^-$, and result in more "free" Li+.[39,41] The additional PEO-cleated Li+ will then improve the segmental motion of PEO chains by crystallinity disruption, enhancing the overall ionic conductivity.

2.5. Different Improving Mechanisms of Active Fillers in PEO-based CSEs

To conclude, the ion pathways in PEO-LATP and PEO-LLZTO CSEs are proposed in **Figure 5**a,b, respectively. Benefitting from the affinity between PEO and LATP, the ion decoupling process

is accelerated and favorable low-resistant PEO/LATP interface, allowing ion transport through bulk LATP. Therefore, LATP serves as bulk-active fillers to provide additional inorganic ion pathways, and Li⁺ transport takes place in both organic and inorganic phases.^[34] In regards to PEO-LL, although the high activation energy of Li⁺ conduction at the PEO/LLZTO interface impedes the bulk Li⁺ transfer, the highly active surface of LLZTO assists in the dissociation of Li-salt, which eventually facilitates improved PEO segment movement. In this sense, LLZTO can be seen as surface-active fillers to enhance the overall ionic conductivity by dissociation effect.

Combining the Li+ pathway and ionic conductivities of the CSEs, the dependences of ionic conductivity on filler content for PEO-based CSEs with bulk-active fillers and surface-active fillers are proposed. As illustrated in Figure 5c, exhibiting higher bulk ionic conductivity than PEO, bulk-active fillers provide additional "fast tracks" for Li+ so the ionic conductivity of CSE continuously increases with filler content and reaches the highest at medium-content-region. However, in spite of the additional ion pathway facilitated by ceramics, the ionic conductivity decreases at higher filler ratios. Because when filler particles become the main component of the CSE, the content of PEO is insufficient to fully cover the surface of fillers, leading to severe phase separation. As for surface-active fillers like LLZTO, although the dissociation effect of surface-active fillers can release more free Li ions for higher ionic conductivity, the poorlymatched PEO/ceramic interface cuts off the ion transfer between organic and inorganic phases. As shown in Figure 5d, the highest ionic conductivity of PEO-LL locates at low-filler-content region. Above such a threshold, the active surface of fillers becomes excessive so that the additional fillers become inactive components. leading to a decrease in overall ionic conductivity. The dramatic

nelibrary.wiley.com/doi/10.1002/smll.202305326 by University Town Of Shenzhen, Wiley Online Library on [23/11/2025]. See the Terms

and Conditions (https://onlinelibrary.wiley.com/terms

conditions) on Wiley Online Library for rules of use; OA articles are governed by the applicable Creative Commons License

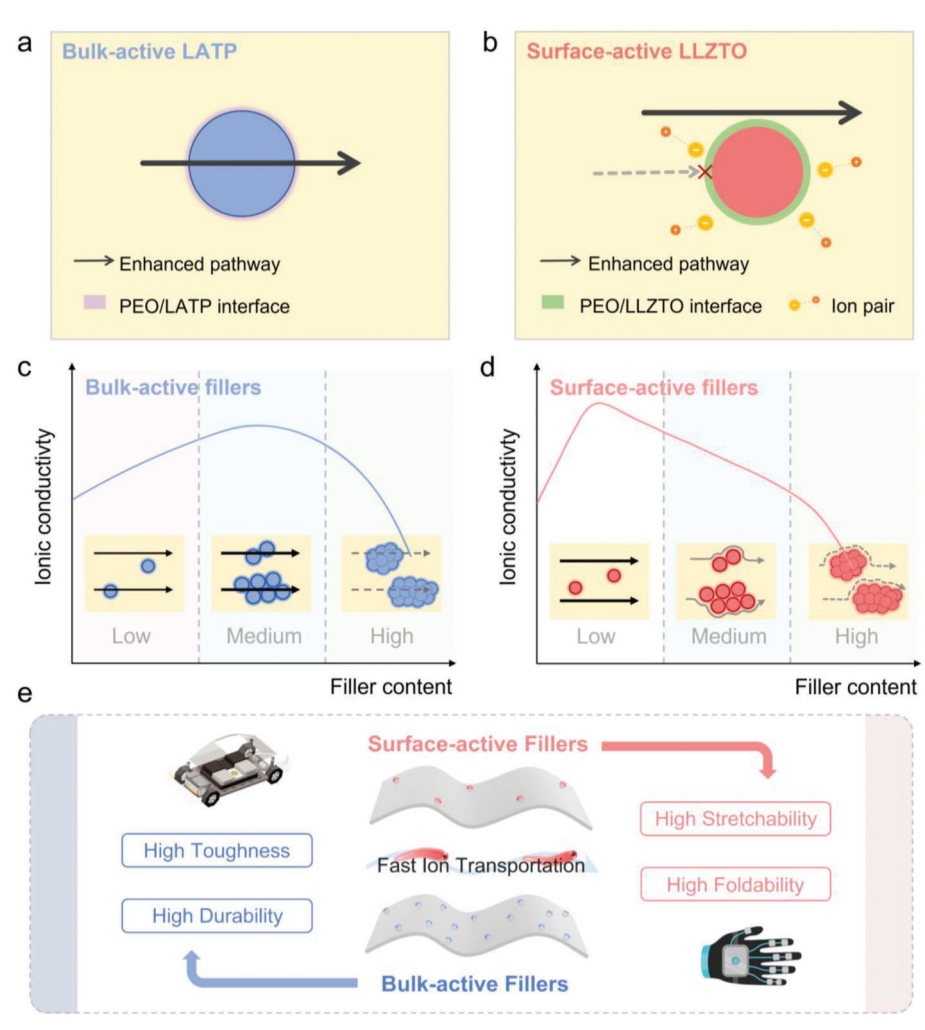


Figure 5. Schematic of Li⁺ pathway for a) PEO-LATP and b) PEO-LLZTO. Proposed dependence of ionic conductivity on filler content for PEO-based CSEs with c) bulk-active fillers and d) surface-active fillers. e) Proposed application scenarios of CSEs using bulk-active and surface-active fillers.

decline in high-filler-content region also corresponds to the seriously limited ion conduction of PEO matrix caused by phase separation.

Since the content of ionic fillers has a great impact on mechanical properties of CSEs, benefiting from the above findings, a new design principle for CSEs is proposed (Figure 5e). Specifically, CSEs with high ionic conductivity should meet the mechanical requirements of the application scenarios. For cases where a huge mechanical impact is expected during operation, such as in electric vehicles, CSEs containing a medium content of bulkactive fillers are more suitable choices due to their high mechanical strength and durability. By contrast, in cases where frequent physical deformation is required during operation, such as in wearable devices and bioelectronics, CSEs with a low content of surface-active fillers are preferred due to their high flexibility and stretchability.

3. Conclusion

In summary, by investigating the correlation between the ionic conductivity and the inorganic filler content in PEO-LATP and PEO-LLZTO CSEs, two types of active fillers are revealed. Surface-active fillers (e. g. LLZTO) improve Li+ conductivity in CSEs by promoting Li-salt dissociation in PEO domains, and their poor affinity toward PEO results in huge interfacial resistance that prevents Li⁺ transport through ceramic bulk. Hence, the ionic conductivity of PEO-LLZTO peaks at a low filler content (10 wt%). The decrease with higher filler content results from the limited ion conduction of PEO matrix hindered by insulating ceramic particles. By contrast, showing good interfacial compatibility with PEO, bulk-active fillers (e.g., LATP) enable a facile Li+ decoupling process from PEO, hence the favorable ion transfer across the PEO-ceramic interface. Consequently, faster Li+ transfer pathways are facilitated in bulk ceramic particles. Therefore, the ionic conductivity for PEO-LATP peaks at the medium-filler content (50 wt%), and the subsequent decline results from severe phase separation. Based on the features of these two different types of active fillers, we have offered a fresh perspective on componential design of highperformance solid-state batteries under various application scenarios. It should be noted that this classification is not absolute, as many active fillers can be both surface and bulk active.

Not to mention that the same filler can be surface active when coupled with one SPE, and becomes bulk active with a different SPE.

4. Experimental Section

Material Preparation: Nano-sized LATP and LLZTO particles with an average diameter of 300 nm were directly purchased from MTI. PEO powders (Mw = 600 000) were purchased from Aldrich. LiTFSI and anhydrous acetonitrile (99%) were purchased from Aladdin. All materials were used without extra purification.

Preparation for Solid Composite Electrolytes: PEO, LiTFSI, and LATP/LLZTO with a series of weight ratios are mixed in anhydrous acetonitrile and mechanically stirred for 12 h at 70 °C in the argon-filled glove box to get a homogeneous solution. And then the solution was casted with a doctor blade on the polytetrafluoroethylene (PTFE) plate and dried at 80 °C for 12 h in the glove box to ensure full solvent evaporation. The weight ratios of PEO to LiTFSI were fixed to 15:4 according to -EO:Li = 24:1. For a typical fabrication for PEO-10LL/LA, 0.144 g LiTFSI, 0.54 g PEO and 0.06 g LLZTO/LATP were mixed in 12 mL anhydrous acetonitrile, followed by subsequent preparation

Preparation for Multilayers PEO-LATP/LLZTP-PEO Symmetric Solid Electrolyte: Ceramic powders are pressed into pellets with a diameter of 12 mm, and the white pellets are sintered in an alumina crucible at a specific temperature for 10 h (950 °C for LATP and 1100 °C for LLZTO) to obtain inorganic pellets. The pellets were polished to 1 mm thick using sandpaper and then stored in an Ar-filled glove box to prevent reaction with humidity and CO₂. Two pieces of 60 µm PEO-LiTFSI thin films were placed on both surfaces of LATP/LLZTO pellet to fabricate PEO-LATP/LLZTO-PEO multilayer electrolytes. The electrolytes were heated to 80 °C for 4 h to ensure intact contact between PEO and LATP/LLZTO pellet.

Materials Characterizations: DSC tests were conducted on the Mettler Toledo in the temperature range from 20 °C to 120 °C at a heating rate of 10 $\mathrm{min^{-1}}$ under N_2 atmosphere. Raman tests were conducted on the Xplora plus Raman spectrometer (HORIBA) with an excitation wavelength of 785 nm. FTIR spectra were collected on a Nicolet Avatar 360 spectrophotometer (ATR)

SAXS measurements were performed at an X-ray scattering instrument (Xeuss 3.0) with an accessible q range from 0.07 to 2.3 nm $^{-1}$. Small angle X-ray scattering transpired when the system under investigation encompasses heterogeneity that differs in electron density from its surroundings. The SAXS intensity I(g) is a function of the scattering angle (2θ) and the wavelength (λ) of the applied radiation, as explicated by the given formula (1).

$$I(q) = 4\pi (\Delta \rho)^2 V \int_0^\infty r^2 \gamma(r) \frac{\sin qr}{ar} dr$$
 (1)

where $q = 4\pi \sin\theta/\lambda$; V represents the volume of the system where X-rays are scattered by electrons. Function $\gamma(r)$ corresponds to the average electron density difference, $\Delta \rho$ induced by different phases. The SAXS intensity I(q) is thus determined by $\Delta \rho$, while the distribution of I(q) was associated with γ (r). In unison, this meant the existence of unequally distributed phases might alter the average electron density, which could be detected and represented on a SAXS profile. Consequently, SAXS was commonly employed to analyze inhomogeneous regions of electron density, and variations in the curve, indicate the non-uniformity of the electrolyte. [42] As indicated in Figure 3f,g, the intensity of scattering peaks indicates the difference in phase separation of the CSEs.

Electrochemical Testing: The CSEs or multilayer electrolytes were sandwiched by two pieces of Φ 16mm stainless-steel disks and assembled in coin cells for EIS tests. As for LATP/LLZTO pellet, gold was deposited onto both sides of the ceramic pellet by vapor deposition as electrodes. The ionic conductivity was evaluated by AC impedance spectra in the frequency range from 1 MHz to 0.1 Hz between 30 °C to 100 °C using an electrochemical workstation (Solartron 1470E). The ionic conductivities (σ) were calculated by the following equation:

$$\sigma = \frac{L}{SR} \tag{2}$$

where S is the area of the contacting surface of the stainless-steel disk with the membranes, L is the total thickness of the membranes and R is the resistance of the membranes.

The activation energy $(E_{\rm a})$ are calculated by the following

$$\sigma (T) = Aexp\left(\frac{-Ea}{kT}\right) \tag{3}$$

where A is a pre-exponential factor. T is the absolute temperature, k refers to Boltzmann constant, and E_2 is the activation energy.

Simulation Methods: The PEO polymer chain was optimized on the Gaussian09 package at $B3LYP^{[43,44]}/6-31+G**$ level of theory. The energy barrier of various reaction processes was carried out based on density functional theory (DFT) in the Vienna ab initio simulation package (VASP)^[45] with projector-augmented wave (PAW) potentials.^[46] The cutoff energy was set to 520 eV. The convergence criteria for the electronic selfconsistent iteration and force were set to 10^{-4} eV and 0.02 eV Å⁻¹, respectively. The exchange-correlation interaction was treated within the generalized gradient approximation (GGA) of Perdew-Burke-Ernzerhof (PBE).^[47] The DFT-D3 method was applied for the Van der Waals (vdW) corrections. The equilibrium lattice constants of structures were optimized when using a $1 \times 1 \times 1$ Monkhorst-Pack k-point grid for Brillouin zone sampling. The Climbing Image-Nudged Elastic Band method was employed to calculate the Li⁺ migration barriers in the structures.

Supporting Information

Supporting Information is available from the Wiley Online Library or from the author.

Acknowledgements

This research was financially supported by Ministry of Science and Technology of China (2016YFB0700600) and Shenzhen Science and Technology Innovation Committee (ISGG20220831095604008).

Conflict of Interest

The authors declare no conflict of interest.

Data Availability Statement

Research data are not shared.

Keywords

active fillers, composite solid electrolytes, ionic conductivity, Li-ion pathways

> Received: June 26, 2023 Revised: July 18, 2023 Published online: July 27, 2023

/onlinelibrary.wiley.com/doi/10.1002/smll.202305326 by University Town Of Shenzhen, Wiley Online Library on [23/11/2025]. See the Terms and Conditions (https://onlinelibrary.wiley.com/term

conditions) on Wiley Online Library for rules

of use; OA articles

are governed by the applicable Creative Commons

- [1] L. Z. Fan, H. He, C. W. Nan, Nat. Rev. Mater. 2021, 6, 1003.
- [2] J. Janek, W. G. Zeier, Nat. Energy 2023, 8, 230.
- [3] Q. Zhao, S. Stalin, C. Z. Zhao, L. A. Archer, Nat. Rev. Mater. 2020, 5, 229
- [4] J. Yan, D. Zhu, H. Ye, H. Sun, X. Zhang, J. Yao, J. Chen, L. Geng, Y. Su, P. Zhang, Q. Dai, Z. Wang, J. Wang, J. Zhao, Z. Rong, H. Li, B. Guo, S. Ichikawa, D. Gao, L. Zhang, J. Huang, Y. Tang, ACS Energy Lett. 2022,
- [5] H. Song, S. Xue, S. Chen, Z. Wang, Y. Song, J. Li, Z. Song, L. Yang, F. Pan, Chin. J. Struct. Chem. 2022, 41, 2205048.
- [6] T. Famprikis, P. Canepa, J. A. Dawson, M. S. Islam, C. Masquelier, Nat. Mater. 2019, 18, 1278.
- [7] Y. Wang, Y. Wu, Z. Wang, L. Chen, H. Li, F. Wu, J. Mater. Chem. A 2022, 10, 4517.
- [8] Y. Song, L. Yang, W. Zhao, Z. Wang, Y. Zhao, Z. Wang, Q. Zhao, H. Liu, F. Pan, Adv. Energy Mater. 2019, 9, 1900671.
- [9] S. Liu, M. Liu, Q. Xu, G. Zeng, Chin. J. Struct. Chem. 2022, 41,
- [10] G. Xi, M. Xiao, S. Wang, D. Han, Y. Li, Y. Meng, Adv. Funct. Mater. **2021**, 31, 2007598.
- [11] J. Mindemark, M. J. Lacey, T. Bowden, D. Brandell, Prog. Polym. Sci. **2018**. 81. 114.
- [12] Y. Ji, K. Yang, M. Liu, S. Chen, X. Liu, B. Yang, Z. Wang, W. Huang, Z. Song, S. Xue, Y. Fu, L. Yang, T. S. Miller, F. Pan, Adv. Funct. Mater. **2021**, 31, 202104830.
- [13] Z. Shen, Y. Cheng, S. Sun, X. Ke, L. Liu, Z. Shi, Carbon Energy 2021, 3,
- [14] Y. Fu, K. Yang, S. Xue, W. Li, S. Chen, Y. Song, Z. Song, W. Zhao, Y. Zhao, F. Pan, L. Yang, X. Sun, Adv. Funct. Mater. 2023, 33, 202210845.
- [15] Z. Li, J. Fu, X. Zhou, S. Gui, L. Wei, H. Yang, H. Li, X. Guo, Adv. Sci. **2023**, 10, 2201718.
- [16] X. Yu, A. Manthiram, Energy Storage Mater. 2021, 34, 282.
- [17] J. Zheng, H. Dang, X. Feng, P. H. Chien, Y. Y. Hu, J. Mater. Chem. A 2017, 5, 18457.
- J. Zheng, M. Tang, Y. Y. Hu, Angew. Chemie Int. Ed. 2016, 55, 12538.
- [19] Z. Li, H. M. Huang, J. K. Zhu, J. F. Wu, H. Yang, L. Wei, X. Guo, ACS Appl. Mater. Interfaces 2019, 11, 784.
- [20] W. Wang, E. Yi, A. J. Fici, R. M. Laine, J. Kieffer, J. Phys. Chem. C 2017, 121, 2563.
- [21] L. Yang, Z. Wang, Y. Feng, R. Tan, Y. Zuo, R. Gao, Y. Zhao, L. Han, Z. Wang, F. Pan, Adv. Energy Mater. 2017, 7, 1701437.
- [22] G. Wang, H. Liu, Y. Liang, C. Wang, L. Z. Fan, Energy Storage Mater. **2022**, 45, 1212.

- [23] K. Lee, S. Han, J. Lee, S. Lee, J. Kim, Y. Ko, S. Kim, K. Yoon, J. H. Song, J. H. Noh, K. Kang, ACS Energy Lett. 2022, 7, 381.
- [24] M. D. Singh, A. Dalvi, D. M. Phase, Y. Kumar, J. Mater. Sci. 2020, 55, 3951.
- [25] L. Chen, Y. Li, S. P. Li, L. Z. Fan, C. W. Nan, J. B. Goodenough, Nano Energy 2018, 46, 176.
- [26] Y. Guo, J. Cheng, Z. Zeng, Y. Li, H. Zhang, D. Li, L. Ci, ACS Appl. Energy Mater. 2022, 5, 2853.
- [27] M. J. Lee, D. O. Shin, J. Y. Kim, J. Oh, S. H. Kang, J. Kim, K. M. Kim, Y. M. Lee, S. O. Kim, Y. G. Lee, Energy Storage Mater. 2021, 37, 306.
- [28] C. Wang, K. Fu, S. P. Kammampata, D. W. McOwen, A. J. Samson, L. Zhang, G. T. Hitz, A. M. Nolan, E. D. Wachsman, Y. Mo, V. Thangadurai, L. Hu, Chem. Rev. 2020, 120, 4257.
- [29] F. Sun, Y. Xiang, Q. Sun, G. Zhong, M. N. Banis, Y. Liu, R. Li, R. Fu, M. Zheng, T. K. Sham, Y. Yang, X. Sun, X. Sun, Adv. Funct. Mater. 2021, 31, 2102129.
- [30] W. E. Tenhaeff, K. A. Perry, N. J. Dudney, J. Electrochem. Soc. 2012, 159, A2118.
- [31] R. F. Samsinger, S. O. Schopf, J. Schuhmacher, P. Treis, M. Schneider, A. Roters, A. Kwade, J. Electrochem. Soc. 2020, 167, 120538.
- [32] E. Trevisanello, T. Ates, S. Passerini, F. H. Richter, J. Janek, J. Electrochem. Soc. 2022, 169, 110547.
- [33] D. Brogioli, F. Langer, R. Kun, F. L. Mantia, ACS Appl. Mater. Interfaces 2019, 11, 11999.
- [34] M. Dinachandra Singh, A. Dalvi, Appl. Surf. Sci. 2021, 536, 147792.
- [35] S. Issa, R. Jeanne-Brou, S. Mehan, D. Devaux, F. Cousin, D. Gigmes, R. Bouchet, T. N. T. Phan, Polymers (Basel) 2022, 14, 5328.
- [36] E. Quartarone, P. Mustarelli, Chem. Soc. Rev. 2011, 40, 2525.
- [37] Y. Zhang, W. Feng, Y. Zhen, P. Zhao, X. Wang, L. Li, Ionics (Kiel) 2022, 28, 2751.
- [38] H. Chen, D. Adekoya, L. Hencz, J. Ma, S. Chen, C. Yan, H. Zhao, G. Cui, S. Zhang, Adv. Energy Mater. 2020, 10, 202000049.
- [39] Y. Song, L. Yang, J. Li, M. Zhang, Y. Wang, S. Li, S. Chen, K. Yang, K. Xu, F. Pan, Small 2021, 17, 2102039.
- [40] H. Xu, R. Hu, H. Yan, B. Li, Z. Cao, Z. Du, Y. Gong, S. Yang, B. Li, ACS Energy Lett. 2022, 7, 3761.
- [41] S. Batteries, N. Wu, P. Chien, Y. Qian, Y. Li, H. Xu, N. S. Grundish, B. Xu, H. Jin, Y. Hu, G. Yu, J. B. Goodenough, 2020, 32306, 4131.
- [42] Q. Sun, S. Wang, Y. Ma, D. Song, H. Zhang, X. Shi, N. Zhang, L. Zhang, Adv. Mater. 2023, 35, 2300998.
- [43] M. Karplus, J Chem Phys 1959, 30, 926.
- [44] T. Lecklider, EE Eval. Eng. 2011, 50, 36.
- [45] L. Filipovic, S. Selberherr, Microelectron. Eng. 2013, 107, 23.
- [46] P. E. Blöchl, Phys. Rev. B 1994, 50, 17953.
- [47] J. P. Perdew, K. Burke, M. Ernzerhof, Phys. Rev. Lett. 1996, 77, 3865.